

Superradiance and subradiance in inverted atomic arrays

Oriol Rubies-Bigorda^{1,2,*} and Susanne F. Yelin²

¹*Physics Department, Massachusetts Institute of Technology, Cambridge, Massachusetts 02139, USA*

²*Department of Physics, Harvard University, Cambridge, Massachusetts 02138, USA*

Superradiance and subradiance are collective effects that emerge from coherent interactions between quantum emitters. Due to their many-body nature, theoretical studies of extended samples with length larger than the atomic transition wavelength are usually restricted to their early time behavior or to the few-excitation limit. We hereby use a mean-field approach to reduce the complex many-body system to an effective two-atom master equation that includes all correlations up to second order and that can be numerically propagated in time. We find that three-dimensional and two-dimensional inverted atomic arrays sustain superradiance below a critical lattice spacing and quantify the scaling of the superradiant peak for both dimensionalities. Finally, we study the late-time dynamics of the system and demonstrate that a subradiant phase appears before the system finally relaxes.

The decay and interaction of dilute ensembles of two-level atoms with the radiation field is commonly described by the semiclassical Maxwell-Bloch equations, which assume the atoms to emit independently and result in an exponential decay of the atomic excitation. While this approximation is accurate when emitters are separated by large distances, it breaks down for dense media. As first noted by Dicke, the photon emitted by one atom can coherently interact with close-by atoms and therefore stimulate emission of additional photons [1–3]. As a result, the atomic dipoles lock in phase, build up coherences and collectively emit at a higher rate, giving rise to the *superradiant burst* in Fig. 1(a). This phenomenon has been experimentally observed in a wide variety of systems, ranging from thermal gases [4–6] to Bose-Einstein condensates [7, 8] and Rydberg atoms [9–11].

In the simplest model, one assumes all atoms to lie in the same spatial position, such that they cannot be distinguished. Then, the N -atom system can only be in one of the $N+1$ symmetric states and the maximum intensity of the emitted light pulse for an initially inverted sample scales with N^2 [1, 3], as opposed to the linear scaling characteristic of independent emitters. In extended samples larger than one atomic transition wavelength, dipole-dipole interactions between different atoms become relevant and the aforementioned symmetry is broken. As a result, the whole Hilbert space with dimension 2^N needs to be considered and most theoretical studies of superradiance and subradiance are consequently restricted to the emission of few photons [12–17] or to systems with a small number of atoms [18–20] such that numerical Monte-Carlo type methods can be applied.

The recent experimental advances in optical lattices [21–23] and atomic tweezers [24–26], which allow to produce atomic lattices —as well as more complex configurations— with inter-particle spacing of the order of an atomic transition wavelength, have revived the interest in superradiant and subradiant physics. While

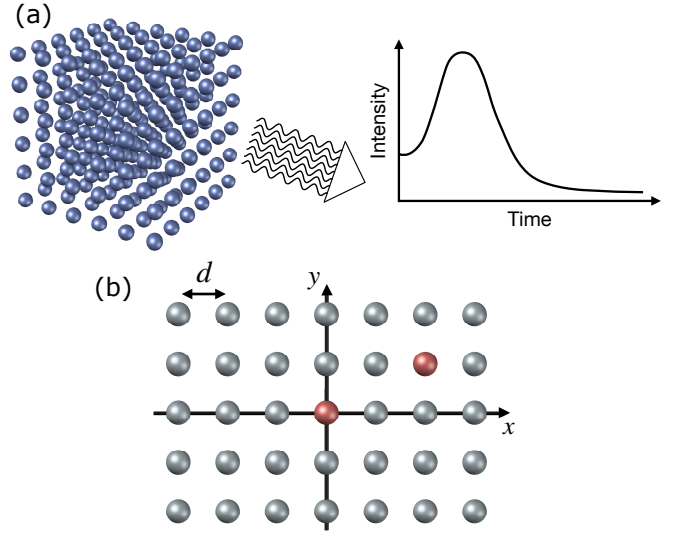


FIG. 1. Superradiance in atomic arrays (a) Collective emission of light from a three-dimensional array of closely-spaced, dipole-coupled atomic emitters. The radiated intensity grows at early times, giving rise to the superradiant burst. (b) Two-dimensional atomic array with inter-particle spacing d . The two red atoms represent the probe atoms used in our formalism to describe the whole system.

these systems have been extensively studied in the case where only one excitation is present in the lattice [27–34], the behavior of inverted lattices is poorly understood. Recent theoretical studies have shown that the appearance of the superradiant burst in inverted samples is determined by the statistics of the first two photons [35, 36], or alternatively by the Taylor series expansion of the photon emission rate at time $t = 0$ [37]. While these methods allow to determine the superradiant phase diagram and the initial slope of the emitted radiation, they provide no information about the scaling of the superradiant peak or the nature of the subsequent time evolution.

In this work, we use an alternative method developed in Refs. [38–40] based on a mean-field approach that includes all correlations up to second order. By tracing

* orubies@mit.edu

out the degrees of freedom of $N - 2$ atoms and the radiation field, one can reduce the description of the full many-body system to an effective non-linear two-atom master equation, which can be numerically propagated in time. We hereby confirm the appearance of a super-radiant burst in two-dimensional and three-dimensional atomic arrays with small enough inter-particle spacing and extend the results in Refs. [35–37] by characterizing the scaling of the superradiant peak for both dimensionalities and by studying the long-time dynamics of the system—which exhibit a subradiant behavior.

We first present the formalism that models the interaction of the atomic array and reduces its description to a two-atom master equation (see Refs. [38–40] for a full derivation). We consider an ensemble of N two-level atoms that interact with the vacuum electromagnetic field. The Hamiltonian of the system consists of three terms: the free Hamiltonian of the atoms H_{at} , the free Hamiltonian of the field H_{field} and the interaction term in the dipole approximation $H_{int} = -\sum_i \vec{p}_i \vec{E}(\vec{r}_i)$, where the index i labels the lattice atoms, \vec{p} is the dipole operator and $\vec{E}(\vec{r}_i)$ represents the quantized field at the atomic positions. Then, two probe atoms 1 and 2 are selected (as illustrated by the two red particles in Fig. 1(b)) and the Hamiltonian is split in two parts $H = H_0 + V$ such that V contains the interaction of the two atoms with the field and H_0 includes the rest of the terms

$$\begin{aligned} H_0 &= H_{at} + H_{field} - \sum_{i \neq 1,2} \vec{p}_i \vec{E}(\vec{r}_i) \\ V &= - \sum_{i=1,2} \vec{p}_i \vec{E}(\vec{r}_i) \end{aligned} \quad (1)$$

Moving to the interaction picture and tracing over the environment degrees of freedom—that is, the radiation field and the $N - 2$ non-selected atoms—one can obtain the effective time evolution operator of the reduced system on the Schwinger-Keldysh contour [41]. Using the Markov and the rotating-wave approximations and keeping correlations up to second order finally results in a master equation for the two probe atoms.

We consider that the two-level atoms have only one transition and that they are initially randomly polarized. Also, we neglect retardation effects of the electromagnetic field and drop the coordinate dependence of the two-atom density matrix by averaging over atom pairs (see Appendix B). The dynamics of the system are then described by three simple quantities: the average upper-level population $a = \rho_{ee,ee} + (\rho_{ee,gg} + \rho_{gg,ee})/2$, the effective two-atom inversion $n = \rho_{ee,ee} - \rho_{ee,gg} - \rho_{gg,ee} + \rho_{gg,gg}$ and the two-atom coherence $\rho_{eg,ge}$. Here, we have defined the density matrix elements $\rho_{\alpha\beta,\gamma\delta} = \langle \alpha_1 \gamma_2 | \rho | \beta_1 \delta_2 \rangle$. The resulting equations of motion are

$$\begin{aligned} \dot{a} &= -(2\Gamma + \gamma)a + \Gamma \\ \dot{n} &= -2(2\Gamma + \gamma)n - 2\gamma(2a - 1) + 8\bar{\Gamma}\rho_{eg,ge} \\ \dot{\rho}_{eg,ge} &= -(2\Gamma + \gamma)\rho_{eg,ge} + \bar{\Gamma}n \end{aligned} \quad (2)$$

where γ is the spontaneous decay rate of a single atom and Γ and $\bar{\Gamma}$ are the one-atom and two-atom cooperative decay rates arising from the interaction with the remaining $N - 2$ atoms mediated by the electromagnetic field. They therefore depend on the retarded Green's function of the atomic medium, as well as on the state of the system (a , n and $\rho_{eg,ge}$) and are ultimately responsible for the superradiant burst. Their exact expressions are given in Appendix B. Thus, Eq. (2) together with the expressions for Γ and $\bar{\Gamma}$ form a self-consistent set of equations that can be propagated in time to obtain the dynamics of the system. Note that, additionally, the interaction between the atoms generates a cooperative energy shift. Because such shifts are generally small in two-level atoms [42], we hereby set it to zero.

The retarded Green's function in the medium describes the propagation of the electromagnetic field in the presence of the ensemble of atoms and therefore depends on the dimension of the system. It can be obtained from the free space Greens function and the polarization of the medium by means of the Dyson equation formalism [43], as described in Appendix A. For a three-dimensional ensemble of randomly polarized atoms, it can be written as

$$\begin{aligned} \tilde{D}_{3D}^{ret}(r) &= -\frac{i\hbar k_0^2 e^{-ik_0 r} e^{\xi r}}{6\pi\epsilon_0 r} \\ \xi &= \gamma \frac{2a - 1}{\gamma/2 + \Gamma} \frac{\pi}{k_0^2 d^3} \end{aligned} \quad (3)$$

where d is the lattice spacing, $k_0 = 2\pi/\lambda$ is the wave number associated to the atomic transition wavelength λ and $r = \sqrt{x^2 + y^2 + z^2}$. In a two-dimensional medium such that all atoms are at $z = 0$, it takes the form

$$\begin{aligned} \tilde{D}_{2D}^{ret}(\rho) &= -\frac{i\hbar k_0}{6\pi\epsilon_0} \int_0^\infty dq \frac{q J_0(q\rho)}{\sqrt{q^2/k_0^2 - 1 + 2i\epsilon/k_0} - i\chi} \\ \chi &= \gamma \frac{2a - 1}{\gamma/2 + \Gamma} \frac{\pi}{k_0^2 d^2} \end{aligned} \quad (4)$$

where $\rho = \sqrt{x^2 + y^2}$ is the distance on the plane defined by the two-dimensional array and the small, positive constant ϵ ensures the convergence of the integral.

Both Green's functions are complex valued, oscillate with distance and their absolute values are increasing functions of the upper-level population a . Whereas the two-dimensional Green's function in the medium $\tilde{D}_{2D}^{ret}(\rho)$ decreases with distance ρ for all values of a , its three-dimensional counterpart $\tilde{D}_{3D}^{ret}(r)$ increases with distance r for $a > 1/2$. In that case, the three-dimensional atomic array turns into an amplifying medium.

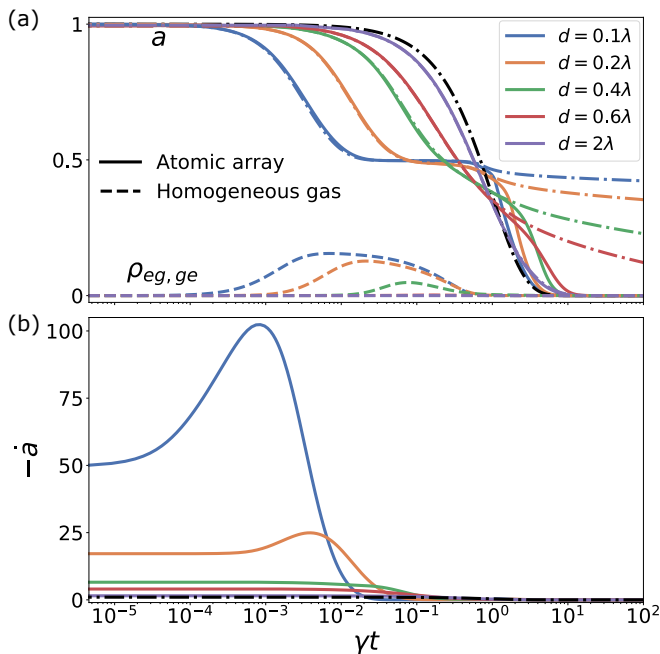


FIG. 2. **Time evolution of three-dimensional atomic arrays** (a) Average upper-level population a (solid lines) and two-atom coherence $\rho_{eg,ge}$ (dashed lines) as a function of time for a spherical, three-dimensional atomic array with $N_{rad} = 25$ particles in the radial direction (and 7153 atoms in total) and for different inter-particle spacings d . The black curve represents the decay in the absence of interactions between particles, that is it recovers the limit $d/\lambda \rightarrow \infty$. The dotted-dashed traces represent the dynamics for an homogeneous spherical gas of atoms with same radius and atomic density. The two-atom coherence is nearly identical in both cases. (b) Intensity per particle $-\dot{a}$ as a function of time for atomic arrays with different spacings. Same color code as in panel (a).

Fig. 2(a) shows the resulting dynamics for a spherical, three-dimensional atomic array with $N_{rad} = 25$ particles in the radial direction. For a small inter-particle spacing of $d = 0.1\lambda$, the average upper-level population a (solid blue curve) initially decays at a much faster rate than would occur for non-interacting particles (black curve). The decay rate or emitted intensity per particle $-\dot{a}$, given by the blue trace in Fig. 2(b), increases at early times and a superradiant burst appears. This substantial increase of emission results from the build-up of coherences in the system, as illustrated by the two-particle coherence $\rho_{eg,ge}$ (dashed blue curve in Fig. 2(a)). After the initial superradiant decay, a subradiant phase appears. The emitted intensity is heavily suppressed and the average upper-level population remains roughly constant, while the coherences build up during the superradiant burst slowly decay. As soon as no coherence remain in the system, the atoms decay and finally reach the ground state.

If the distance d between the nearest-neighbors in the lattice is increased, these effects get weaker. More con-

cretely, the superradiant burst decreases and disappears above a certain critical spacing d_{crit} , the maximum two-particle coherence is reduced and the subradiant phase vanishes. For inter-particle distances much larger than the atomic transition wavelength, as it is the case of the purple curve with $d = 2\lambda$, the non-interacting case is recovered. That is, the atomic dipoles do not build up coherences and simply decay exponentially at the fixed rate γ .

The time evolution of the two probe atoms can be further used to characterize the superradiant peak. The inset in Fig. 3(a) shows the intensity per particle during the burst for three-dimensional arrays of spacing $d = 0.1\lambda$ and different number of particles along the radial direction N_{rad} . The magnitude of the peak $-\dot{a}_{max}$ increases with lattice size and the point at which the emission is maximum t_{max} shifts to earlier times. The exact scaling of both features depends on two quantities: the characteristic length or size of the array, given by $N_{rad}d$; and the number of particles within a cubic atomic transition wavelength d^{-3} , which corresponds to the density of the sample and coincides with the relevant length scale that appears in the three-dimensional retarded Green's function through the parameter ξ given in Eq. (3). For a three-dimensional ensemble, its product results in the optical depth of the medium $\mathcal{O} = N_{rad}/d^2$. As illustrated in Fig. 3, the maximum emission rate per particle scales linearly with the optical depth $-\dot{a}_{max} \propto \mathcal{O}$, whereas the time at which the maximum emission occurs is inversely proportional to it $t_{max} \propto \mathcal{O}^{-1}$. Thus, the total peak intensity scales as $N^{4/3}$, well below the typical N^2 -scaling found in the Dicke limit, where all atoms are contained in a volume much smaller than λ^3 . Note that the optical depth of a sample with a fixed number of atoms depends on the specific shape of the system. Samples with a preferential axis, such as cigar-shaped clouds, have a smaller amount of transverse photon modes [44] and can therefore attain a quadratic dependence of the pulse intensity with atom number [45]. Additionally, such samples do not scatter photons in all directions as it is the case for spherical arrays or clouds [46], but emit light predominantly along the preferential directions with highest optical depth [7, 45].

Defining that a superradiant burst occurs if the emitted intensity per particle initially increases, that is if $-d^2a/dt^2 > 0$, one can obtain the superradiant phase diagram for three-dimensional atomic arrays in Fig. 4(a). A burst appears below a critical inter-particle spacing d_{crit} , that is if the medium is dense enough. The spacing d_{crit} depends on the size of the array, such that larger samples can sustain superradiance at larger lattice constants. Note that these values are much lower than those reported in other references [35–37] and have to be understood as a very conservative estimate. This is due to the self-consistent procedure used to compute the cooperative rate Γ , which considers interactions and cooperativity to be present from the beginning. As a result, the initial decay rate $-\dot{a}(t = 0)$ is overestimated

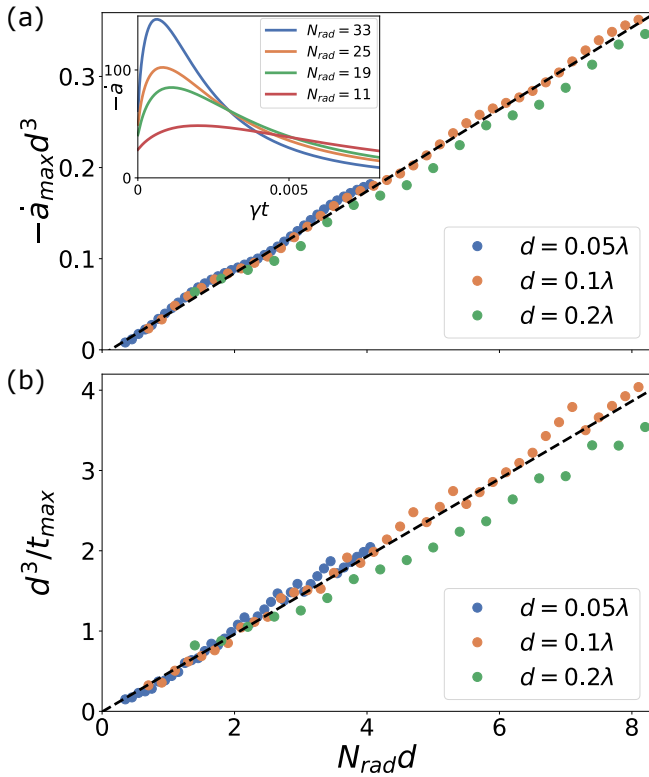


FIG. 3. **Superradiant peak for a three-dimensional array** (a) Maximum emission rate $-\dot{a}_{max}$ multiplied by d^3 versus radius or characteristic length of the sample $N_{rad}d$ for different lattice spacings d . The inset shows the emitted intensity per particle as a function of time for atomic arrays with fixed $d = 0.1\lambda$ and different N_{rad} . (b) Time at which the maximum emission occurs versus sample radius and for different spacings. As shown by the black linear fits, $-\dot{a}_{max}$ scales with N_{rad}/d^2 and t_{max} with d^2/N_{rad} .

and masks the appearance of a burst at finite time if the superradiant peak is not prominent enough. Alternatively, one can obtain a more realistic estimate of the critical spacing by using the scaling of the superradiant peak $-\dot{a}_{max}d^2 \approx f(N_{rad})$, where f is a linear function of the number of atoms in the radial direction. For a certain N_{rad} , d_{crit} corresponds to the spacing that results in $-\dot{a}_{max}^{crit} = 1$, that is, $d_{crit} = d\sqrt{-\dot{a}_{max}}$. Fig. 4(b) shows the resulting phase diagram extracted from the traces in Fig. 3(a), which qualitatively matches those reported in Refs. [35–37]. For both phase diagrams, we obtain a critical spacing that scales as $d_{crit} \propto \sqrt{N_{rad}}$ [37], as shown by the black dashed fitted curves.

Interestingly, the early dynamics (superradiant and subradiant phases) of the atomic array are very similar to those of a three-dimensional, homogeneous gas of atoms with the same size and density of particles [39, 40], as shown in Fig. 2(a). More specifically, an identical scaling of the superradiant peak and a similar phase diagram as the one shown in Fig. 4 are found for a homogeneous gas. However, the late dynamics differ consider-

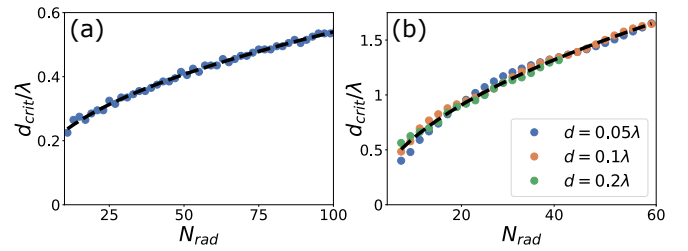


FIG. 4. **Phase diagram for a three-dimensional array** (a) Maximum spacing d_{crit} at which superradiance is sustained as a function of system size N_{rad} . A burst is considered to occur if the emitted intensity per particle initially grows, that is, if $-d^2 a/dt^2 > 0$. (b) Phase diagram estimated from the scaling of the superradiant peak $-\dot{a}_{max}d^2 \approx f(N_{rad})$. Using the traces in Fig. 3(a), the critical spacing for a given N_{rad} is obtained as $d_{crit} = d\sqrt{-\dot{a}_{max}}$. The dashed black curves are fittings of the form $d_{crit} = a + b\sqrt{N_{rad}}$.

ably. While the partially excited, ordered atomic array rapidly decays once the coherences between atoms vanish, the excitation remains in the system much longer in the case of an homogeneous gas of atoms, giving rise to a radiation trapping regime [47–49]. When more than half of the excitation has been emitted, that is $a < 1/2$, the three-dimensional Green’s function in the medium \tilde{D}_{3D}^{ret} becomes absorbing and its value decays with distance. Thus, the interaction predominantly occurs between nearest neighbors. Even if the average spacing between the atoms in the gas is of the order of a wavelength, there is a non-negligible chance that some atoms are found to be much closer than that. This gives rise to an enhanced interaction in the gas and therefore a larger collective decay rate Γ , which ultimately suppresses emission according to Eq. (2).

For two-dimensional atomic arrays, that is ensembles of atoms lying on a plane, the time evolution of the average upper-level population a and the two-level coherence $\rho_{eg,ge}$ presents the same three regimes as the three-dimensional case in Fig. 2(a). However, the two-dimensional superradiant burst is weaker, the subradiant phase is less prominent and both collective effects emerge only at lower inter-particle spacings, consistent with the fact that three-dimensional lattices are better packed geometries containing many more particles within a cubic transition wavelength. We consider two ways of computing the two-atom cooperative decay rate $\bar{\Gamma}$: $\bar{\Gamma}^{(A)}$, which corresponds to the case where both probe atoms are nearest neighbors; and $\bar{\Gamma}^{(C)}$, the averaged decay rate over atom pairs defined in Appendix B that has so far been used to study the behavior of three-dimensional arrays. Fig. 5(a) depicts the emission rate $-\dot{a}$ for small samples ($N_{rad} = 21$) of various spacings and shows the appearance of a superradiant burst at low enough d . For a fixed spacing, however, the maximum emission rate $-\dot{a}_{max}$ does not monotonically increase with sample size, but oscillates with period 2λ , as illustrated in Fig. 5(b). That is, a maximum (or minimum) is reached every time the

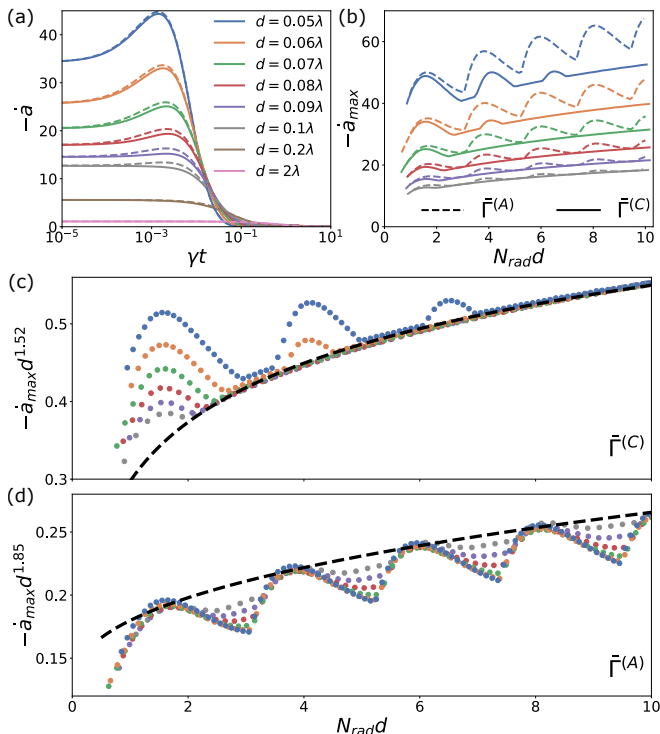


FIG. 5. **Superradiant peak for a two-dimensional array** (a) Intensity per particle $-\dot{a}$ emitted by a two-dimensional atomic array as a function of time for different lattice constants d . A circular sample with $N_{rad} = 21$ particles in the radial direction (317 atoms in total) is considered. (b) Maximum intensity per particle $-\dot{a}_{max}$ for samples with different N_{rad} and d . Same colorscale in all panels. Dashed lines correspond to the two-atom cooperative decay rate $\bar{\Gamma}^{(A)}$, whereas solid lines represent the result for $\bar{\Gamma}^{(C)}$ (see Appendix B). (c) Scaling of the superradiant peak resulting from $\bar{\Gamma}^{(C)}$. The black curve corresponds to a fit of the form $-\dot{a}_{max}d^{1.52} \propto \log(N_{rad}d)$. An equally good fitting can be obtained with the power-law $-\dot{a}_{max}d^{1.52} \propto (N_{rad}d)^{0.23}$. (d) Scaling of the superradiant peak resulting from $\bar{\Gamma}^{(A)}$. The black curve corresponds to a fit of the form $-\dot{a}_{max}d^{1.85} \propto (N_{rad}d)^{0.4}$.

radius of the atomic array increases by one atomic transition wavelength. This behavior arises from the oscillating nature of the retarded Green’s function in the medium, which results in constructive and destructive interference between the different “shells” of the array when computing the cooperative decay rates Γ and $\bar{\Gamma}$. Note that these oscillations also appear in three-dimensional arrays (see Fig. 3(a)), although their effect is much weaker due to the strongly amplifying nature of the three-dimensional medium. It is also worth noting that the atomic coherences in the two-dimensional medium decay with distance (between probe atoms). As a result, the averaged $\bar{\Gamma}^{(C)}$ is lower than the nearest-neighbor version $\bar{\Gamma}^{(A)}$ (see Appendix D) and the resulting $-\dot{a}_{max}$ is thus larger in the later case.

The functional form of $-\dot{a}_{max}$ can be obtained by ap-

propriately scaling the emission axis. Fig. 5(c) shows that the maximum emission rate obtained with $\bar{\Gamma}^{(C)}$ scales as $-\dot{a}_{max}d^{1.52} \propto \log(N_{rad}d)$, consistent with the logarithmic scaling with atom number found in Ref. [37] for the initial slope of the total radiation. Note that an alternative power-law scaling of the form $-\dot{a}_{max}d^{1.52} \propto (N_{rad}d)^{0.23}$ provides an equally good fitting. A similar scaling is obtained for the minima of $-\dot{a}_{max}$ computed with $\bar{\Gamma}^{(A)}$ (see Appendix D). As for the maxima, the traces in Fig. 5(d) can be fitted with the power law $-\dot{a}_{max}d^{1.85} \propto (N_{rad}d)^{0.4}$. These results suggest that the total peak intensity in two-dimensional arrays scales as $N \log(N^{1/2})$, or alternatively with a power law N^α with exponent $\alpha \in \{1.115, 1.2\}$ smaller than that of three-dimensional arrays and of the Dicke case.

In conclusion, we have analyzed the many-body dynamics of closely-spaced and dipole-coupled atomic arrays by means of a reduced two-atom master equation that captures correlations with the rest of the ensemble. As opposed to the formalism used in Refs. [35–37], which perfectly captures the photon emission at zero time, our method overestimates the initial cooperative effects in the array and consequently does not provide accurate estimates of the superradiant phase diagrams. However, it satisfactorily captures the mid- and long-term behavior of the atomic system. This allows us not only to demonstrate the appearance of superradiance and subradiance below a critical spacing, but also to characterize the scaling of the superradiant peak for three-dimensional and two-dimensional atomic arrays. We additionally show that the figures of merit for the superradiant burst of ordered arrays and homogeneous gases of atoms are similar, and identify significant differences in the late-time dynamics of both systems. As opposed to arrays, homogeneous gases can sustain radiation trapping once the atomic coherences vanish due to non-zero probability of finding two atoms at distances much lower than the average inter-particle spacing.

The collective phenomena studied in this paper may be experimentally realized in a wide variety of platforms, ranging from ultracold atoms trapped in optical lattices [21, 50] and tweezers [25, 26] to condensed matter systems such as quantum emitters in two-dimensional materials [51, 52] or vacancy centers in bulk crystals [53–55]. Further, this work could be extended by adding a classical driving field, which may elucidate the behavior of arrays in other regimes of the multi-excitation sector for which theoretical and numerical understanding is still very limited [37, 56, 57]. Also, the effective two-atom description of the many-body problem can be potentially leveraged to study other systems or reservoirs by appropriately modifying the Green’s function of the medium [58].

We thank Hanzhen Ma for insightful conversations about the effective two-atom model used to describe the atomic arrays. We also acknowledge valuable discussions with Ana Asenjo-Garcia and Stuart J. Masson. This work has been supported by the NSF through The CUA

Physics Frontier Center, and through PHY-1912607, as well as by the AFOSR through the grant FA9550-19-1-0233. ORB acknowledges support from Fundació Bancària “la Caixa” (LCF/BQ/AA18/11680093).

Appendix A: Retarded Green’s function in the medium

The retarded Green’s function in the medium is obtained from the free-space Green’s function D_0^{ret} and the polarization source function P^{ret} using the Dyson equation formalism [38, 43], which is graphically represented in Fig. 6. It can be formally written as

$$D_{\alpha\beta}^{ret}(\vec{r}_1, t_1; \vec{r}_2, t_2) = D_{0\alpha\beta}^{ret}(\vec{r}_1, t_1; \vec{r}_2, t_2) - \int_{-\infty}^{\infty} dt'_1 \int_{-\infty}^{\infty} dt'_2 \times \int_V d^3r'_1 D_{0\alpha\mu}^{ret}(\vec{r}_1, t_1; \vec{r}'_1, t'_1) P_{\mu\nu}^{ret}(\vec{r}'_1, t'_1, t'_2) D_{\nu\beta}^{ret}(\vec{r}'_1, t'_2; \vec{r}_2, t_2) \quad (\text{A1})$$

where α, β represent the components of the Green’s tensor.

The polarization function P^{ret} is given by the correlation function of dipole operators of non-interacting atoms, which can be computed using the quantum regression theorem [39]. Using a continuum approximation, P^{ret} can be expressed as

$$P^{ret}(\vec{r}, t) = \frac{\wp^2}{\hbar^2} \frac{1}{d^{\mathcal{D}}} \frac{2a(\vec{r}, t) - 1}{\gamma/2 + \Gamma} \quad (\text{A2})$$

where d is the lattice constant, a is the average upper-level population of the two probe atoms, Γ is the cooperative decay rate and \mathcal{D} represents the dimensionality of the array, that is $\mathcal{D} = 3$ for three-dimensional lattices and $\mathcal{D} = 2$ for two-dimensional ones.

Eq. (A1) can be solved in Fourier space if a series of approximations are done [38]. First, we extend the spatial integral to infinity. Second, the spatial dependence of the source function is replaced by \vec{r}_2 . Finally, we make use of the Markov approximation to only keep the slow time dependence of the source function and assume that it depends on the time difference $t'_1 - t'_2$. We can then Fourier transform with respect to space $\vec{x} = \vec{r}_1 - \vec{r}_2$ and time $\tau = t_1 - t_2$ and obtain

$$\overline{\overline{D^{ret}}} = \overline{D_0^{ret}} + \overline{D_0^{ret}} \circlearrowleft P^{ret} \overline{\overline{D^{ret}}}$$

FIG. 6. Graphical representation of the Dyson equation. The retarded Green’s function inside the medium D^{ret} is generated by the free-space Green’s function D_0^{ret} and the polarization source function P^{ret} .

$$\tilde{\tilde{D}}^{ret}(\vec{q}, \omega; t) = \left[\mathbf{1} + \tilde{\tilde{D}}_0^{ret}(\vec{q}, \omega) \tilde{\tilde{P}}^{ret}(\omega; t) \right]^{-1} \tilde{\tilde{D}}_0^{ret}(\vec{q}, \omega) \quad (\text{A3})$$

where $\tilde{\tilde{D}}^{ret}$ and $\tilde{\tilde{P}}^{ret}$ are 3x3 matrices and $\mathbf{1}$ is the identity matrix.

The free-space retarded Green’s function in real space is

$$\tilde{D}_{0\alpha\beta}^{ret}(\vec{x}, k_0) = -\frac{i\hbar}{4\pi\epsilon_0} \left(k_0^2 \delta_{\alpha\beta} + \frac{\partial^2}{\partial x_\alpha \partial x_\beta} \right) \frac{e^{-ik_0 r}}{r} \quad (\text{A4})$$

where $r = |\vec{x}|$. If the medium is randomly polarized, one can apply the polarization average $\langle \wp_\alpha \wp_\beta \rangle = \frac{1}{3} \delta_{\alpha\beta}$. This is equivalent to performing the orientation average $x_\alpha x_\beta / r^2 \rightarrow \langle x_\alpha x_\beta / r^2 \rangle = \frac{1}{3} \delta_{\alpha\beta}$. The Green’s function then becomes a spherical tensor with components

$$\tilde{D}_0^{ret}(\vec{x}, k_0) = -\frac{i\hbar k_0^2}{6\pi\epsilon_0} \frac{e^{-ik_0 r}}{r} \quad (\text{A5})$$

with $k_0 = 2\pi/\lambda$. The spherical nature of the problem now simplifies Eq. (A3) to the scalar equation

$$\tilde{\tilde{D}}^{ret}(\vec{q}, k_0) = \frac{1}{\left(\tilde{\tilde{D}}_0^{ret}(q, k) \right)^{-1} + P^{ret}} \quad (\text{A6})$$

$\tilde{\tilde{D}}_0^{ret}(\vec{q}, k_0)$ is obtained by Fourier transforming Eq. (A5) and it therefore depends on the dimensionality of the sample.

1. Three-dimensional sample

For a three-dimensional sample, the free-space Green’s function in momentum space is

$$\tilde{\tilde{D}}_0^{ret}(\vec{q}, k_0) = -\frac{2i\hbar k_0^2}{3\epsilon_0} \frac{1}{q^2 - k_0^2 + 2ik_0\epsilon} \quad (\text{A7})$$

where the small, positive constant ϵ moves the pole at $q = k_0$ to the lower half of the complex plane. Plugging this result in Eq. (A6), performing the inverse Fourier transform with respect to \vec{q} and inserting the explicit form of the source function given by Eq. (A2), one finally obtains Eq. (3) of the main text [38]

$$\tilde{D}_{3D}^{ret}(r) = -\frac{i\hbar k_0^2}{6\pi\epsilon_0} \frac{e^{-ik_0 r} e^{\xi r}}{r} \quad (\text{A8})$$

$$\xi = \gamma \frac{2a - 1}{\gamma/2 + \Gamma} \frac{\pi}{k_0^2 d^3}$$

where we have defined the spontaneous decay rate $\gamma = \wp^2 k_0^3 / 3\pi\epsilon_0 \hbar$.

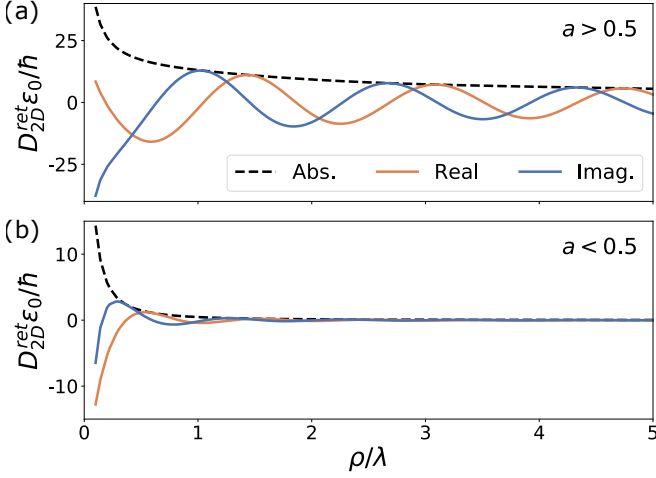


FIG. 7. **Two-dimensional retarded Green's function** Retarded Green's function in a two-dimensional medium $\tilde{D}_{2D}^{ret}\epsilon_0/\hbar$ as a function of distance for (a) $a > 0.5$ and $\chi = 0.8$ and (b) $a < 0.5$ and $\chi = -0.8$. The orange and blue traces correspond to the real and imaginary parts respectively, whereas the dashed black line represents the absolute value. A spacing of $d = 0.1\lambda$ is considered.

Thus, the Green's function in a three-dimensional medium oscillates with period λ . For a predominantly excited medium such that the average upper-level population $a > 0.5$, ξ is positive and \tilde{D}_{3D}^{ret} exponentially increases with distance. In this regime, the medium is amplifying. For $a < 0.5$, the medium becomes absorbing and \tilde{D}_{3D}^{ret} decreases with distance.

2. Two-dimensional sample

We assume that the atomic sample is located in the xy-plane, such that $z = 0$ for all atoms. Then, the Fourier transform is carried out only over x and y and the retarded free-space Green's function in momentum space is

$$\tilde{D}_0^{ret}(\vec{q}, z = 0, k_0) = -\frac{i\hbar k_0}{3\epsilon_0} \frac{1}{\sqrt{q^2/k_0^2 - 1 + 2i\epsilon/k_0}} \quad (\text{A9})$$

where the momentum is now defined in two dimensions $\vec{q} = (k_x, k_y)$ and $q = \sqrt{q_x^2 + q_y^2}$. Again, a small, positive constant ϵ is introduced.

From Eq. (A6) and Eq. (A2), it follows

$$\tilde{D}_{2D}^{ret}(\vec{q}, k_0) = -\frac{i\hbar k_0}{3\epsilon_0} \frac{1}{\sqrt{q^2/k_0^2 - 1 + 2i\epsilon/k_0 - i\chi}} \quad (\text{A10})$$

where we have defined the parameter

$$\chi = \frac{\gamma}{\gamma/2 + \Gamma} \frac{\pi}{k_0^2 d^2} (2a - 1) \quad (\text{A11})$$

that depends on the state of the two probe atoms and the lattice constant of the array. Performing the inverse Fourier transform, we obtain

$$\begin{aligned} \tilde{D}_{2D}^{ret}(\rho, z = 0) &= \frac{1}{(2\pi)^2} \int_{-\infty}^{\infty} dq_x \int_{-\infty}^{\infty} dq_y \tilde{D}^{ret}(\vec{q}, k_0) e^{-i\vec{q}\vec{r}} \\ &= \frac{1}{(2\pi)^2} \int_0^{2\pi} d\theta \int_0^{\infty} q dq \tilde{D}^{ret}(\vec{q}, k_0) e^{-iq\rho \cos\theta} \\ &= -\frac{i\hbar k_0}{6\pi\epsilon_0} \int_0^{\infty} dq \frac{q J_0(q\rho)}{\sqrt{q^2/k_0^2 - 1 + 2i\epsilon/k_0 - i\chi}} \end{aligned} \quad (\text{A12})$$

where J_0 is the zeroth order Bessel function of the first kind and $\rho = \sqrt{x^2 + y^2}$ is the distance between two points on the xy-plane.

The integral is performed numerically for the discrete set of distances ρ that appear in an atomic array. That is, given a lattice with spacing d , one needs to consider $\rho = d\sqrt{n_x^2 + n_y^2}$, where n_x and n_y are integers. Note also that Eq. (A12) has a pole at $q = \pm k_0\sqrt{1 - \chi^2}$. The small constant ϵ therefore ensures the convergence of the integral when the pole is located in the real axis.

As shown in Fig. 7, $\tilde{D}_{2D}^{ret}(\rho)$ oscillates and its absolute value decays with distance for all values of χ . That is, the medium is absorbing for all average upper-level populations a .

Appendix B: Cooperative decay rates

After tracing out the degrees of freedom of the electromagnetic field and the $N - 2$ non-selected atoms, the resulting master equation for the reduced system—and therefore the equations of motion given by Eq. (2)—depend on the cooperative decay rates Γ and $\bar{\Gamma}$. These quantities can be expressed in terms of the two-time cumulants of the field operators and are therefore related to the Green's function in the atomic medium. As shown in Refs. [39, 40], one can find the closed form expressions

$$\begin{aligned}
\Gamma(\vec{r}) &= \frac{\wp^4}{\hbar^4} \sum_{\vec{x}} \frac{2a(\vec{x})}{\gamma/2 + \Gamma} \left| \tilde{D}^{ret}(\vec{r} - \vec{x}) \right|^2 + \frac{\wp^4}{\hbar^4} \sum_{\vec{x}_1} \sum_{\vec{x}_2} \frac{2\rho_{eg,ge}(\vec{x}_1 - \vec{x}_2)}{\gamma/2 + \Gamma} \tilde{D}^{ret}(\vec{r} - \vec{x}_1) \tilde{D}^{*ret}(\vec{r} - \vec{x}_2) \\
\bar{\Gamma}(\vec{r}_1, \vec{r}_2) &= \frac{\wp^4}{\hbar^4} \sum_{\vec{x}} \frac{2a(\vec{x})}{\gamma/2 + \Gamma} \tilde{D}^{ret}(\vec{r}_1 - \vec{x}) \tilde{D}^{*ret}(\vec{r}_2 - \vec{x}) + \frac{\wp^4}{\hbar^4} \sum_{\vec{x}_1} \sum_{\vec{x}_2} \frac{2\rho_{eg,ge}(\vec{x}_1 - \vec{x}_2)}{\gamma/2 + \Gamma} \tilde{D}^{ret}(\vec{r}_1 - \vec{x}_1) \tilde{D}^{*ret}(\vec{r}_2 - \vec{x}_2)
\end{aligned} \tag{B1}$$

where the summation is carried out over all the atoms of the system, located at positions \vec{x} . The specific form of the retarded Green's function depends on the dimensionality of the lattice and the decay rates depend on the positions of the two probe atoms. Γ and $\bar{\Gamma}$ can be understood as the one-atom and two-atom cooperative decay rates, respectively. That is, Γ appears in the reduced master equation through terms involving raising and lowering operators of one probe atom only (e.g. $\sigma_1\sigma_1^\dagger$), while $\bar{\Gamma}$ corresponds to terms that involve both probe atoms (e.g. $\sigma_1\sigma_2^\dagger$). Note also that the decay rates for an homogeneous gas can be obtained by replacing $\sum_{\vec{x}} \rightarrow \mathcal{N} \int_V d^3\vec{x}$, where \mathcal{N} denotes the density of the medium [39, 40]. For clarity, we define $\Gamma = \Gamma_1 + \Gamma_2$ and $\bar{\Gamma} = \bar{\Gamma}_1 + \bar{\Gamma}_2$, where the subindexes indicate the first and second term of both collective decay rates.

We hereby assume that the spatial dependence of the atomic variables is much weaker than that of the field correlations, which rapidly oscillate according to \tilde{D}^{ret} . We thus describe the atomic system with the averaged variables a , n and $\rho_{eg,ge}$. Additionally, we consider that the one-atom cooperative decay rate can be approximated as $\Gamma \approx \Gamma(\vec{r} = \vec{0})$, consistent with the fact that in large enough samples the majority of the atoms are deep inside the array. Similarly, $\bar{\Gamma}_2$ is approximated as $\sum_{\vec{x}_1} \tilde{D}^{ret}(\vec{r}_1 - \vec{x}_1) \sum_{\vec{x}_2} \tilde{D}^{*ret}(\vec{r}_2 - \vec{x}_2) \approx \sum_{\vec{x}} \left| \tilde{D}^{ret}(\vec{x}) \right|^2$ and is therefore equal to Γ_2 . However, $\bar{\Gamma}_1$ strongly depends on the choice of \vec{r}_1 and \vec{r}_2 , as the addends in $\sum_{\vec{x}} \tilde{D}^{ret}(\vec{r}_1 - \vec{x}) \tilde{D}^{*ret}(\vec{r}_2 - \vec{x})$ interfere differently depending on the exact value of both quantities. We will hereby consider three different ways of computing $\bar{\Gamma}$:

- (A) $\bar{\Gamma}_1^{(A)} = \bar{\Gamma}_1(\vec{r}_1 = \vec{0}, \vec{r}_2)$: Decay rate for a specific pair of atoms. Unless otherwise stated, we will consider nearest neighbors such that $\vec{r}_1 = \vec{0}$ and $|\vec{r}_2 - \vec{r}_1| = d$.
- (B) $\bar{\Gamma}_1^{(B)} = \frac{1}{N} \sum_{\vec{r}_2 \neq \vec{0}} \bar{\Gamma}_1(\vec{r}_1 = \vec{0}, \vec{r}_2)$: Average over all possible atom pairs, considering that one of the atoms is at the center of the array.
- (C) $\bar{\Gamma}_1^{(C)} = \frac{1}{N} \frac{\wp^4}{\hbar^4} \frac{2a}{\gamma/2 + \Gamma} \left| \sum_{\vec{x}} \tilde{D}^{ret}(\vec{x}) \right|^2$: Alternative average introduced in Ref. [39], which results from adding an extra summation $\frac{1}{N} \sum_{\vec{x}_2}$ and thus separating the \vec{x} -dependence into two different variables \vec{x}_1 and \vec{x}_2 .

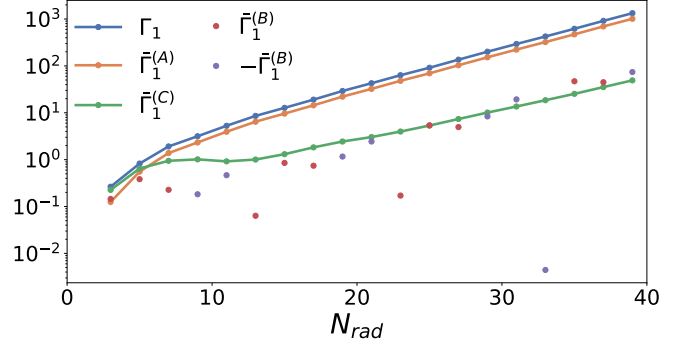


FIG. 8. $\bar{\Gamma}_1$ in a three-dimensional array $\Gamma_1/\gamma^2 a$ (blue) and $\bar{\Gamma}_1/\gamma^2 a$ as a function of number of atoms in the radial direction N_{rad} for an array with $d = 0.2\lambda$ and $\Gamma = 10\gamma$. The different colors correspond to the different ways of computing $\bar{\Gamma}_1$: $\bar{\Gamma}_1^{(A)}/\gamma^2 a$ in orange (with $|\vec{r}_2 - \vec{r}_1| = d$), $\bar{\Gamma}_1^{(B)}/\gamma^2 a$ in red, $-\bar{\Gamma}_1^{(B)}/\gamma^2 a$ in purple and $\bar{\Gamma}_1^{(C)}/\gamma^2 a$ in green.

The results presented in the main text are obtained using $\bar{\Gamma}_1^{(C)}$ in the case of the three-dimensional arrays and $\bar{\Gamma}_1^{(A)}$ and $\bar{\Gamma}_1^{(C)}$ in the case of two-dimensional lattices. Also, the differences between the various ways of computing $\bar{\Gamma}_1$ for both dimensionalities are discussed in Appendix C and Appendix D, respectively.

Appendix C: Three-dimensional array

Fig. 8 shows the different values of $\bar{\Gamma}_1$ obtained for a three-dimensional square lattice with spherical shape. For an individual pair of atoms at positions \vec{r}_1 and \vec{r}_2 , it is simply proportional to $\sum_{\vec{x}} \tilde{D}^{ret}(\vec{r}_1 - \vec{x}) \tilde{D}^{*ret}(\vec{r}_2 - \vec{x})$. Given that the retarded Green's function oscillates with distance, both factors overlap in different ways depending on the relative position of \vec{r}_1 and \vec{r}_2 . If both atoms are at positions such that $\tilde{D}^{ret}(\vec{r}_1)$ and $\tilde{D}^{*ret}(\vec{r}_2)$ have the same sign, the retarded Green's functions overlap in phase and the addends add up constructively. Also, the farther away both atoms are, the smaller is the resulting sum. However, if the signs of $\tilde{D}^{ret}(\vec{r}_1)$ and $\tilde{D}^{*ret}(\vec{r}_2)$ differ, the Green's function at the atomic positions have opposite phases and the resulting $\bar{\Gamma}$ can become negative. This represents a non-physical scenario in which Γ can, in turn, also become negative during the time evolution,

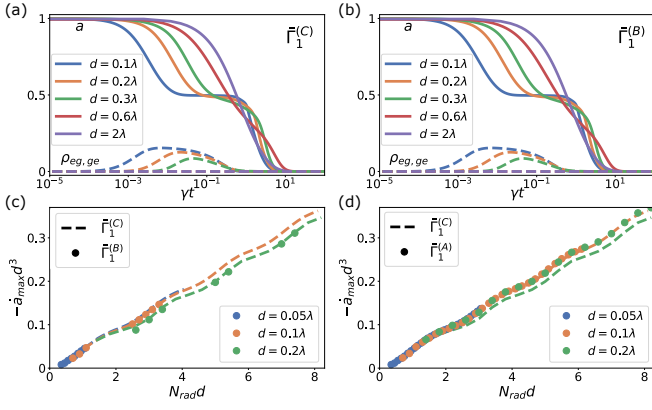


FIG. 9. **Result comparison for three-dimensional arrays** (a)-(b) Average upper-level population a (solid lines) and two-atom coherence $\rho_{eg,ge}$ (dashed lines) as a function of time for a spherical, three-dimensional atomic array with $N_{rad} = 25$ particles in the radial direction and for different lattice constants d . In (a), the expression $\bar{\Gamma}_1^{(C)}$ is used, whereas (b) is obtained with $\bar{\Gamma}_1^{(B)}$. (c)-(d) Maximum emission rate multiplied by d^3 versus radius or characteristic length of the sample $N_{rad}d$ for different values of d . The dashed lines are obtained with $\bar{\Gamma}_1^{(C)}$, whereas the dots correspond to $\bar{\Gamma}_1^{(B)}$ in panel (c) and $\bar{\Gamma}_1^{(A)}$ with $|\vec{r}_2 - \vec{r}_1| = d$ in panel (d).

probably due to an overestimation of the phase coherence over distance.

For $\bar{\Gamma}_1^{(A)}$ such that $|\vec{r}_2 - \vec{r}_1| = d$, there is an almost perfect, constructive overlap and the resulting decay rate (orange trace) is always positive and close to $\Gamma_1 = \bar{\Gamma}_1(\vec{r}_1 = \vec{r}_2)$ (blue trace). Both $\bar{\Gamma}_1^{(B)}$ and $\bar{\Gamma}_1^{(C)}$ represent averages over different atom pairs and their absolute values are therefore smaller than those of Γ_1 or $\bar{\Gamma}_1^{(A)}$. The “usual” average $\bar{\Gamma}_1^{(B)}$ additionally results in regions with positive (red dots) and negative (purple dots) decay rates, which alternate every time the sample size increases by λ . Interestingly, $\bar{\Gamma}_1^{(C)}$ is always positive and is close to the absolute value of $\bar{\Gamma}_1^{(B)}$. Note also that Γ_1 , $\bar{\Gamma}_1^{(A)}$ and $\bar{\Gamma}_1^{(C)}$ only involve a summation over the $N \approx N_{rad}^3$ lattice sites of the array, whereas $\bar{\Gamma}_1^{(B)}$ contains two nested summations which increases the number of operations quadratically and consequently reduces the maximum array size that can be numerically simulated.

The results shown in the main text are obtained using $\bar{\Gamma}_1^{(C)}$. Fig. 9(a)-(b) shows that the resulting dynamics are identical for $\bar{\Gamma}_1^{(C)}$ (panel (a)) and $\bar{\Gamma}_1^{(B)}$ (panel (b)), as long as $\bar{\Gamma}_1^{(B)} > 0$. As for the scaling of the superradiant peak, depicted in Fig. 9(c)-(d), all three versions provide nearly identical results, confirming the scaling with the optical depth $\mathcal{O} = N_{rad}/d^2$ and the slight oscillations arising from the interference between different “shells” of the array.

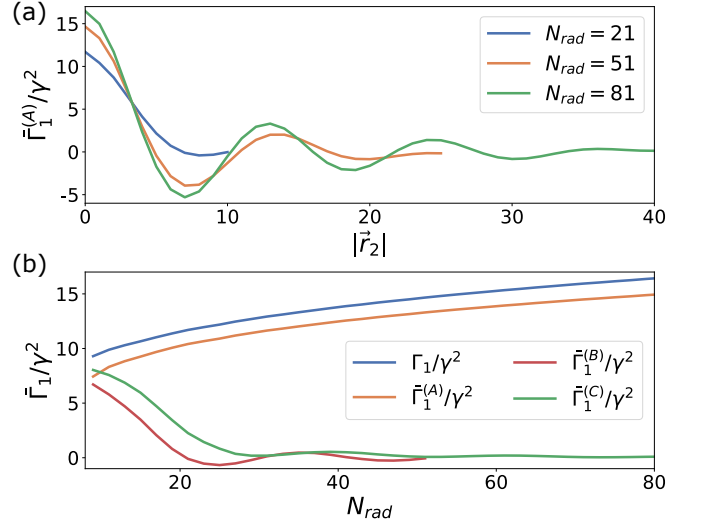


FIG. 10. $\bar{\Gamma}_1$ in a two-dimensional array (a) $\bar{\Gamma}_1^{(A)}(\vec{r}_1 = 0, \vec{r}_2)$ for a two-dimensional, circular array of atoms with spacing $d = 0.1\lambda$ at the positions $\vec{r}_2 = (|\vec{r}_2|, 0)$. The different colors represent arrays of different sizes. (b) Γ_1 (blue trace) and $\bar{\Gamma}_1/\gamma^2$ as a function of number of atoms in the radial direction N_{rad} for an array with $d = 0.1\lambda$. The different colors correspond to the different ways of computing $\bar{\Gamma}_1$: A in orange (with $|\vec{r}_2 - \vec{r}_1| = d$), B in red and C in green. In both panels, we consider an initially inverted array $a = 1$ and the corresponding Γ given by Eq. B1.

Appendix D: Two-dimensional array

Fig. 10(a) shows $\bar{\Gamma}_1^{(A)}(\vec{r}_1 = 0, \vec{r}_2)$ for circular two-dimensional arrays with different sizes N_{rad} as a function of $\vec{r}_2 = (|\vec{r}_2|, 0)$. Again, in-phase and out-of-phase overlaps in the term $\sum_{\vec{x}} \tilde{D}_2^{ret}(\vec{x}) \tilde{D}^{*ret}(\vec{r}_2 - \vec{x})$ result in maxima and minima of $\bar{\Gamma}_1$ and a subsequent oscillating behavior of $\bar{\Gamma}_1$ with the distance between probe atoms. Due to the absorbing nature of the two-dimensional Green’s function, i.e. $\tilde{D}_{2D}^{ret}(\rho)$ decays with distance ρ , the oscillations are damped and the contribution of $\bar{\Gamma}_1$ to the two-atom cooperative decay rate becomes very small for probe atoms that lie far apart.

In Fig. 10(b), we compare the different ways of computing $\bar{\Gamma}_1$ for arrays of various sizes. As can be inferred from Fig. 10(a), $\bar{\Gamma}_1^{(A)}(|\vec{r}_2| = d)$ is a growing function of the sample size and is close to $\Gamma_1 = \bar{\Gamma}_1^{(A)}(|\vec{r}_2| = 0)$. $\bar{\Gamma}_1^{(B)}$ is obtained by averaging over all positions \vec{r}_2 present in the array and decays and oscillates with N_{rad} due to the additional periods that emerge in $\bar{\Gamma}_1^{(A)}(\vec{r}_1 = 0, \vec{r}_2)$ when the sample size is increased. Finally, $\bar{\Gamma}_1^{(C)}$ follows a similar trend as $\bar{\Gamma}_1^{(B)}$.

In the main text, we present the results obtained using both $\bar{\Gamma}_1^{(A)}$ and $\bar{\Gamma}_1^{(C)}$. Note that the fact that $\bar{\Gamma}_1^{(A)} > \bar{\Gamma}_1^{(C)}$ results in larger values of the two-atom coherences and consequently of the superradiant peak for method (A), as shown by Fig. 5(b) in the main text. Also, the oscillations

tions in $\Gamma_2 = \bar{\Gamma}_2 = \bar{\Gamma}_1^{(C)} N \rho_{egge} / a$ lead to an oscillatory behavior of the maximum emission rate $-\dot{a}_{max}$, which can be understood as an interference effect between different “shells” of the array.

Fig. 11 shows the maximum decay rate $-\dot{a}_{max}$ obtained with $\bar{\Gamma}_1^{(A)}$ for arrays with different sizes and spacings. The grey and black curves correspond to fittings of the type $-\dot{a}_{max} \propto \log(N_{rad})$ and $-\dot{a}_{max} \propto N_{rad}^{0.22}$, respectively, and match the scaling obtained in Fig. 5(c) of the main text with $\bar{\Gamma}_1^{(C)}$.

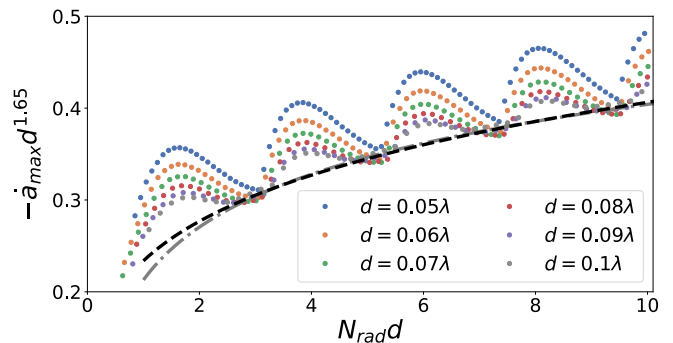


FIG. 11. **Two-dimensional superradiant burst** Scaling of the minima of the superradiant peak resulting from $\bar{\Gamma}_1^{(A)}$. The black curve corresponds to a fit of the form $-\dot{a}_{max} d^{1.65} \propto (N_{rad} d)^{0.22}$ and the grey trace to the functional form $-\dot{a}_{max} d^{1.65} \propto \log(N_{rad} d)$.

-
- [1] R. H. Dicke, Coherence in spontaneous radiation processes, *Phys. Rev.* **93**, 99 (1954).
- [2] R. H. Lehmann, Radiation from an n -atom system. i. general formalism, *Phys. Rev. A* **2**, 883 (1970).
- [3] M. Gross and S. Haroche, *Phys. Rep.* **93**, 301 (1982).
- [4] G. Feher, J. P. Gordon, E. Buehler, E. A. Gere, and C. D. Thurmond, Spontaneous emission of radiation from an electron spin system, *Phys. Rev.* **109**, 221 (1958).
- [5] N. Skribanowitz, I. P. Herman, J. C. MacGillivray, and M. S. Feld, Observation of dicke superradiance in optically pumped hf gas, *Phys. Rev. Lett.* **30**, 309 (1973).
- [6] A. Szöke and S. Meiboom, Radiation damping in nuclear magnetic resonance, *Phys. Rev.* **113**, 585 (1959).
- [7] S. Inouye, A. P. Chikkatur, D. M. Stamper-Kurn, J. Stenger, D. E. Pritchard, and W. Ketterle, Superradiant rayleigh scattering from a bose-einstein condensate, *Science* **285**, 571 (1999).
- [8] K. Baumann, C. Guerlin, F. Brennecke, and T. Esslinger, Dicke quantum phase transition with a superfluid gas in an optical cavity, *Nature* **464**, 1301 (2010).
- [9] T. Wang, S. F. Yelin, R. Côté, E. E. Eyler, S. M. Farooqi, P. L. Gould, M. Koštrun, D. Tong, and D. Vrinceanu, Superradiance in ultracold rydberg gases, *Phys. Rev. A* **75**, 033802 (2007).
- [10] Y. Kaluzny, P. Goy, M. Gross, J. M. Raimond, and S. Haroche, Observation of self-induced rabi oscillations in two-level atoms excited inside a resonant cavity: The ringing regime of superradiance, *Phys. Rev. Lett.* **51**, 1175 (1983).
- [11] D. D. Grimes, S. L. Coy, T. J. Barnum, Y. Zhou, S. F. Yelin, and R. W. Field, Direct single-shot observation of millimeter-wave superradiance in rydberg-rydberg transitions, *Phys. Rev. A* **95**, 043818 (2017).
- [12] T. Bienaimé, N. Piovella, and R. Kaiser, Controlled dicke subradiance from a large cloud of two-level systems, *Phys. Rev. Lett.* **108**, 123602 (2012).
- [13] M. O. Scully, E. S. Fry, C. H. R. Ooi, and K. Wódkiewicz, Directed spontaneous emission from an extended ensemble of n atoms: Timing is everything, *Phys. Rev. Lett.* **96**, 010501 (2006).
- [14] A. Svidzinsky and J.-T. Chang, Cooperative spontaneous emission as a many-body eigenvalue problem, *Phys. Rev. A* **77**, 043833 (2008).
- [15] A. A. Svidzinsky, J.-T. Chang, and M. O. Scully, Cooperative spontaneous emission of n atoms: Many-body eigenstates, the effect of virtual lamb shift processes, and analogy with radiation of n classical oscillators, *Phys. Rev. A* **81**, 053821 (2010).
- [16] X. Kong and A. Pálffy, Collective radiation spectrum for ensembles with zeeman splitting in single-photon superradiance, *Phys. Rev. A* **96**, 033819 (2017).
- [17] F. Cottier, R. Kaiser, and R. Bachelard, Role of disorder in super- and subradiance of cold atomic clouds, *Phys. Rev. A* **98**, 013622 (2018).
- [18] J. P. Clemens, L. Horvath, B. C. Sanders, and H. J. Carmichael, Collective spontaneous emission from a line of atoms, *Phys. Rev. A* **68**, 023809 (2003).
- [19] S. J. Masson, I. Ferrier-Barbut, L. A. Orozco, A. Browaeys, and A. Asenjo-Garcia, Many-body signatures of collective decay in atomic chains, *Phys. Rev. Lett.* **125**, 263601 (2020).
- [20] H. Carmichael and K. Kim, A quantum trajectory unraveling of the superradiance master equation., *Optics Communications* **179**, 417 (2000).
- [21] J. Rui, D. Wei, A. Rubio-Abadal, S. Hollerith, J. Zeiher, D. M. Stamper-Kurn, C. Gross, and I. Bloch, A subradiant optical mirror formed by a single structured atomic layer, *Nature* **583**, 369374 (2020).
- [22] I. Bloch, Ultracold quantum gases in optical lattices, *Nature Physics* **1**, 23 (2005).
- [23] H. Labuhn, D. Barredo, S. Ravets, S. de Léséleuc, T. Macrì, T. Lahaye, and A. Browaeys, Tunable two-dimensional arrays of single rydberg atoms for realizing quantum ising models, *Nature* **534**, 667670 (2016).
- [24] M. Endres, H. Bernien, A. Keesling, H. Levine, E. R. Anschuetz, A. Krajenbrink, C. Senko, V. Vuletic, M. Greiner, and M. D. Lukin, Atom-by-atom assembly of defect-free one-dimensional cold atom arrays, *Science* **354**, 1024 (2016).
- [25] D. Barredo, S. de Léséleuc, V. Lienhard, T. Lahaye, and A. Browaeys, An atom-by-atom assembler of defect-free arbitrary two-dimensional atomic arrays, *Science* **354**,

- 1021 (2016).
- [26] D. Ohl de Mello, D. Schäffner, J. Werkmann, T. Preuschoff, L. Kohfahl, M. Schlosser, and G. Birkl, Defect-free assembly of 2d clusters of more than 100 single-atom quantum systems, *Phys. Rev. Lett.* **122**, 203601 (2019).
- [27] E. Shahmoon, D. S. Wild, M. D. Lukin, and S. F. Yelin, Cooperative resonances in light scattering from two-dimensional atomic arrays, *Phys. Rev. Lett.* **118**, 113601 (2017).
- [28] A. Asenjo-Garcia, M. Moreno-Cardoner, A. Albrecht, H. J. Kimble, and D. E. Chang, Exponential improvement in photon storage fidelities using subradiance and “selective radiance” in atomic arrays, *Phys. Rev. X* **7**, 031024 (2017).
- [29] L. Henriot, J. S. Douglas, D. E. Chang, and A. Albrecht, Critical open-system dynamics in a one-dimensional optical-lattice clock, *Phys. Rev. A* **99**, 023802 (2019).
- [30] M. Moreno-Cardoner, D. Plankensteiner, L. Ostermann, D. E. Chang, and H. Ritsch, Subradiance-enhanced excitation transfer between dipole-coupled nanorings of quantum emitters, *Phys. Rev. A* **100**, 023806 (2019).
- [31] T. L. Patti, D. S. Wild, E. Shahmoon, M. D. Lukin, and S. F. Yelin, Controlling interactions between quantum emitters using atom arrays, *Phys. Rev. Lett.* **126**, 223602 (2021).
- [32] R. J. Bettles, S. A. Gardiner, and C. S. Adams, Cooperative eigenmodes and scattering in one-dimensional atomic arrays, *Phys. Rev. A* **94**, 043844 (2016).
- [33] C. D. Parmee and J. Ruostekoski, Signatures of optical phase transitions in superradiant and subradiant atomic arrays, *Communications Physics* **3**, 205 (2020).
- [34] O. Rubies-Bigorda, V. Walther, T. L. Patti, and S. F. Yelin, Photon control and coherent interactions via lattice dark states in atomic arrays (2021), arXiv:2108.13964.
- [35] S. J. Masson and A. Asenjo-Garcia, Universality of dicke superradiance in atomic arrays (2021), arXiv:2106.02042.
- [36] E. Sierra, S. J. Masson, and A. Asenjo-Garcia, Dicke superradiance in ordered lattices: role of geometry and dimensionality (2021), arXiv:2110.08380.
- [37] F. Robicheaux, Theoretical study of early time superradiance for atom clouds and arrays (2021), arXiv:2110.00498.
- [38] M. Fleischhauer and S. F. Yelin, Radiative atom-atom interactions in optically dense media: Quantum corrections to the lorentz-lorenz formula, *Phys. Rev. A* **59**, 2427 (1999).
- [39] G.-D. Lin and S. F. Yelin, *Adv. At. Mol. Opt. Phys.* **61**, 295 (2012).
- [40] H. Ma, O. Rubies-Bigorda, and S. F. Yelin, Superradiance and subradiance in a gas of two-level atoms, private communication.
- [41] L. V. Keldysh, *Sov. Phys. JETP* **20**, 1018 (1965).
- [42] G. Putnam, G.-D. Lin, and S. F. Yelin, Collective induced superradiant lineshifts, arXiv:1612.04477 (2016).
- [43] F. J. Dyson, The s matrix in quantum electrodynamics, *Phys. Rev.* **75**, 1736 (1949).
- [44] E. Akkermans, A. Gero, and R. Kaiser, Photon localization and dicke superradiance in atomic gases, *Phys. Rev. Lett.* **101**, 103602 (2008).
- [45] J. H. Müller, D. Witthaut, R. le Targat, J. J. Arlt, E. S. Polzik, and A. J. Hilliard, Semi-classical dynamics of superradiant rayleigh scattering in a bose-einstein condensate, *Journal of Modern Optics* **63**, 1886 (2016).
- [46] E. Paradis, B. Barrett, A. Kumarakrishnan, R. Zhang, and G. Raithel, Observation of superfluorescent emissions from laser-cooled atoms, *Phys. Rev. A* **77**, 043419 (2008).
- [47] C. R. Stroud, J. H. Eberly, W. L. Lama, and L. Mandel, Superradiant effects in systems of two-level atoms, *Phys. Rev. A* **5**, 1094 (1972).
- [48] F. W. Cummings and A. Dorri, Exact solution for spontaneous emission in the presence of n atoms, *Phys. Rev. A* **28**, 2282 (1983).
- [49] P. Weiss, M. O. Araújo, R. Kaiser, and W. Guerin, Subradiance and radiation trapping in cold atoms, *New Journal of Physics* **20**, 063024 (2018).
- [50] G. E. Marti, R. B. Hutson, A. Goban, S. L. Campbell, N. Poli, and J. Ye, Imaging optical frequencies with 100 μ Hz precision and 1.1 μ m resolution, *Phys. Rev. Lett.* **120**, 103201 (2018).
- [51] C. Palacios-Berraquero, D. M. Kara, A. R.-P. Montblanch, M. Barbone, P. Latawiec, D. Yoon, A. K. Ott, M. Loncar, A. C. Ferrari, and M. Atatüre, Large-scale quantum-emitter arrays in atomically thin semiconductors, *Nature Communications* **8**, 15093 (2017).
- [52] G. Haider, K. Sampathkumar, T. Verhagen, L. Nádvořník, F. J. Sonia, V. Valeš, J. Sýkora, P. Kapusta, P. Nèmec, M. Hof, O. Frank, Y.-F. Chen, J. Vejpravová, and M. Kalbáč, Superradiant emission from coherent excitons in van der waals heterostructures, *Advanced Functional Materials* **31**, 2102196 (2021).
- [53] F. Feng, J. Wang, W. Zhang, J. Zhang, L. Lou, W. Zhu, and G. Wang, Efficient generation of nanoscale arrays of nitrogen-vacancy centers with long coherence time in diamond, *Applied Physics A* **122**, 944 (2016).
- [54] P. Spinicelli, A. Dréau, L. Rondin, F. Silva, J. Achard, S. Xavier, S. Bansropun, T. Debuisschert, S. Pezzagna, J. Meijer, V. Jacques, and J.-F. Roch, Engineered arrays of nitrogen-vacancy color centers in diamond based on implantation of cn-molecules through nanoapertures, *New Journal of Physics* **13**, 025014 (2011).
- [55] A. Sipahigil, R. E. Evans, D. D. Sukachev, M. J. Burek, J. Borregaard, M. K. Bhaskar, C. T. Nguyen, J. L. Pacheco, H. A. Atikian, C. Meuwly, R. M. Camacho, F. Jelezko, E. Bielejec, H. Park, M. Lončar, and M. D. Lukin, An integrated diamond nanophotonics platform for quantum-optical networks, *Science* **354**, 847 (2016).
- [56] Y.-X. Zhang and K. Mølmer, Universal free-fermion multiply-excited eigenstates and their experimental signatures in 1d arrays of two-level atoms (2021), arXiv:2109.04540.
- [57] S. J. Masson and A. Asenjo-Garcia, Atomic-waveguide quantum electrodynamics, *Phys. Rev. Research* **2**, 043213 (2020).
- [58] D. E. Chang, J. S. Douglas, A. González-Tudela, C.-L. Hung, and H. J. Kimble, Colloquium: Quantum matter built from nanoscopic lattices of atoms and photons, *Rev. Mod. Phys.* **90**, 031002 (2018).